Assessment of the combustion characteristics of hydrogen transverse jets in supersonic crossflow

By M. Gamba, V. E. Terrapon, A. Saghafian, M. G. Mungal AND H. Pitsch

1. Motivation and objectives

In this work we are providing an assessment of the supersonic combustion model developed by Terrapon *et al.* (2009) and Saghafian *et al.* (2011) and integrated into Reynolds averaged Navier-Stoke (RANS) and Large Eddy Simulation (LES) solvers. For this purpose, the experiment of Gamba *et al.* (2011) of a reacting transverse jet in supersonic crossflow is used. The aim of the work is to investigate the structure of the reaction zones in the shear layer, the near-wall burning regions induced by the jet/bow shock interaction (Gamba *et al.* 2011), and to assess how the features observed in the laboratory are predicted by the RANS and LES approaches.

In the following sections, the experimental configuration and a brief description of the experimental approach will be introduced. Then, the combustion model and its implementation in the RANS and LES solvers will be described. Finally, the flow and flame structure, and an assessment of how both RANS and LES approaches approximate them will be discussed.

2. Experimental considerations

In this section a description of the experimental configuration and techniques used for the investigation will be briefly summarized. A more detailed account of the experimental arrangement can be found in Gamba *et al.* (2011).

2.1. *Transverse jet in supersonic crossflow and experimental arrangement*

The flow of interest in the study was generated by a hydrogen jet issued perpendicularly from a flat plate immersed in a crossflow. Figure 1 shows a three-dimensional (3D) schematic diagram of the flat plate and of the flow field resulting from transverse injection into a supersonic crossflow. Fuel was injected through the contoured injector shown schematically in Figure 2. Different cases were considered, but the work presented here is based on the case with a jet plenum pressure $p_{j,o} = 2435\ kPa$, which results in a momentum flux ratio $J = \frac{\rho_{jet} U_{jet}^2}{\rho_\infty U_\infty^2}$ of 5.0 and a jet Reynolds number of 3.2×10^5. The crossflow (air) was generated in the Stanford Expansion Tube. Details on the experimental arrangement and calibration procedure can be found in Gamba *et al.* (2011).

For the flow conditions of the experiment, the 99% boundary layer thickness was estimated to be 1 mm using analytical considerations (White 1991) and qualitative Schlieren imaging. The unit Reynolds number ${}^{U_\infty}/_{\nu_\infty}$ of the crossflow was about $3 \times 10^6\ m^{-1}$ and the local Reynolds number at the injector location was about 2×10^5. Under this condition a laminar boundary layer would be expected (White 1991).

The experiments presented here were conducted at the Stanford 6" Expansion Tube Facility developed and described in detail by Heltsley (Heltsley *et al.* 2006; Heltsley 2011).

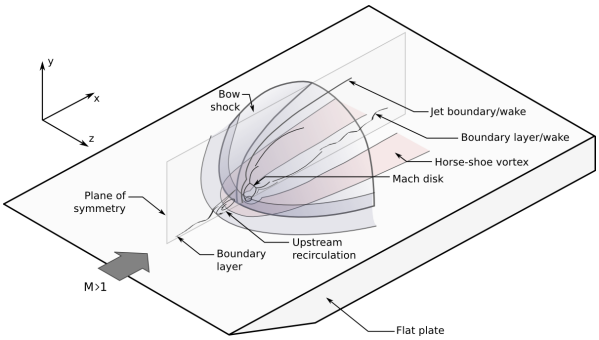

FIGURE 1. Three-dimensional schematic diagram of a transverse jet in supersonic crossflow issued from a flat plate.

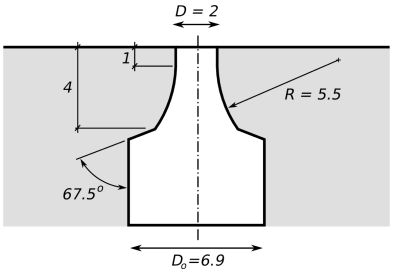

FIGURE 2. Schematic diagram of the contoured injector. Dimensions in *mm*.

A discussion of the operation principle can be found in Trimpi (1962). More specific details regarding the arrangement of the expansion tube for the current experiments can be found in Gamba *et al.* (2011).

The crossflow conditions ($p,\ T,\ M$) were maintained fixed at $p = 40kPa$, $T \approx 1500K$ and $M = 2.4$, with an expected shot-to-shot variation of less than 2.5% of the nominal values. The test time duration was experimentally determined to be approximately $500\mu s$.

Different imaging techniques were used to investigate the flow and reaction zone structure: Schlieren imaging was used to investigate the shock and jet structure, OH^* chemiluminescence imaging was used to investigate ignition and overall flame penetration, and OH planar laser-induced fluorescence (PLIF) was used to mark and investigate the instantaneous reaction zone on several orthogonal planes. Due to the short test time duration, the imaging experiments are single-shot realizations and were carried out at the same nominal time delay with respect to the initiation of the flow, well after a steady state was established.

3. Numerical simulations

The experiment described above has been simulated at RANS and LES levels by Saghafian *et al.* (2011) using the flamelet-based combustion model for the supersonic regime developed in Terrapon *et al.* (2009). In the following sections, a brief overview of the numerical implementation and models will be given.

3.1. *RANS approach*

The RANS solver used for the solution of the compressible Navier-Stokes equations is based on a finite volume formulation and implicit time-integration on arbitrary polyhedral meshes (Pecnik *et al.* 2009; Terrapon *et al.* 2009). The Euler fluxes are computed with an HLLC approximate Riemann solver (Toro *et al.* 1994; Batten *et al.* 1997). Second-order accuracy is typically achieved by computing the states at each side of a given cell face using second-order interpolation and then applying the same flux evaluation scheme to the reconstructed states. Gradients are limited with a modified version of the Barth and Jespersen slope limiter (Pecnik *et al.* 2009; Barth & Jespersen 2011; Venkatakrishnan 1995). The system of conservation equations is solved fully coupled and the resulting large sparse system (the Jacobian matrices are obtained using first-order discretization) is solved with the generalized minimal residual method (GMRES) using

the freely available linear solver package PETSc (Satish *et al.* 2009). The two-equation turbulence model $k-\omega$ SST (Menter 1994) is used to describe turbulence. The turbulent Schmidt and Prandtl numbers are set to 0.5.

For RANS calculations, the computational domain was defined over half of the flat plate domain with uniform inflow, symmetry boundary condition on the center plane of the domain (intersecting the injector), and outflow elsewhere. Because of the short-duration of the experiment, a constant temperature (300 K) boundary condition was imposed at the wall. The 3D RANS mesh contained about 2.2 million cells, with the first mesh point off the wall at $\Delta_y^+ < 1$ to correctly capture the boundary layer. Two limiting cases were considered: (i) the boundary layer was assumed to be initially laminar and transition to turbulence was then imposed at the position of the upstream recirculation bubble (see below); (ii) the boundary layer was assumed to be fully turbulent.

3.2. *LES approach*

The LES solver is based on an energy-conserving unstructured finite volume discretization with explicit third-order Runge-Kutta time integration (Mahesh *et al.* 2004; Ham & Iaccarino 2004). The LES solver has novel operators with minimized numerical dissipation and dispersion errors (Moureau *et al.* 2007; Shoeybi *et al.* 2010). The flux calculation relies on a hybrid central and WENO method in which a shock sensor is used to identify where the WENO scheme should be applied. The solver uses the dynamic Smagorinsky model to close the sub-grid terms in the LES equations (Moin *et al.* 1991).

For LES calculations, the flat plate domain was considered with uniform inflow conditions and constant temperature boundary condition at the wall. The LES mesh contained about 30 million cells. The inflow boundary layer was assumed laminar.

3.3. *Flamelet-based combustion model*

The supersonic combustion model used in the study (Terrapon *et al.* 2009) is based on a flamelet description of the flame structure (Peters 1984; Pitsch 2006). It is based on the Flamelet/Progress Variable (FPV) approach of low-Mach number turbulent non-premixed combustion (Pierce & Moin 2004). Chemistry is pre-computed and tabulated as a series of laminar flamelet solutions for a given set of boundary conditions and background pressure p_o. The non-premixed flamelet solutions are parameterized with respect to the mixture fraction Z and a reaction progress variable C, which is defined here as the mass fraction of water. Assumed Probability Density Functions (PDF) account for turbulence/chemistry interaction. A $\beta-$PDF is assumed for Z and a $\delta-$PDF for C. The local thermochemical state (temperature T and species mass fractions Y_i) is tabulated with the Favre-averaged mixture fraction $\widetilde{Z}$, mixture fraction variance $\widetilde{Z''^2}$, and progress variable $\widetilde{C}$ at constant p_o.

In the low-Mach number approximation, temperature and species mass fractions are assumed to depend only on $\left(\widetilde{Z}, \widetilde{Z''^2}, \widetilde{C}\right)$. However, in the supersonic regime where compressibility and viscous heating effects are important, the internal energy $\widetilde{e}$ computed as part of the flow solution is inconsistent with the internal energy of the tabulated chemistry. This inconsistency is resolved by inferring temperature from $\widetilde{e}$ in a closed form using an approximate linearization of $\widetilde{e}$ about its flamelet solution $\widetilde{e}_o$, where the linearization parameters are tabulated in the flamelet library (Terrapon *et al.* 2010). The error committed by this approximation is about 5 K for a temperature 300 K away from the flamelet solution. However, this approximation does not take into account changes in

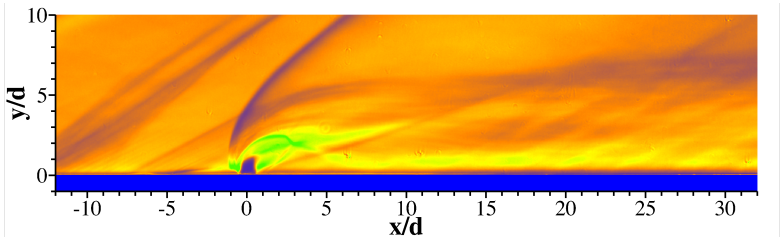

FIGURE 3. Time-averaged (20 μs) Schlieren image of the transverse jet at $J = 5.0$.

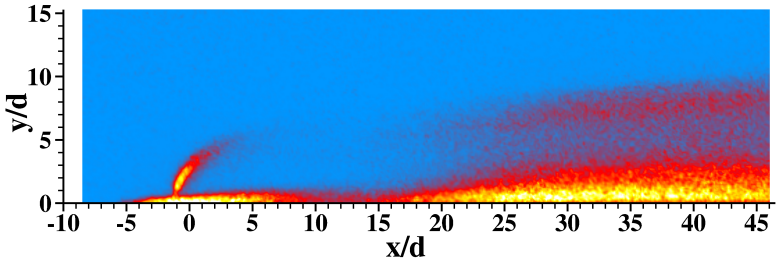

FIGURE 4. Time-averaged (200 μs) OH^* chemiluminscence image for $J = 5.0$ jet.

composition with corrected temperature. Pressure is then computed from the ideal gas law using the corrected temperature.

A pressure rescaling of the source term in the transport equation of C, $\bar{\dot{\omega}}_C$, was assumed and proposed (Terrapon *et al.* 2010; Saghafian *et al.* 2011) as an approximate correction to account for compressibility/chemistry interaction. With this approximation, $\bar{\dot{\omega}}_C$ is rescaled as $\bar{\dot{\omega}}_C = \bar{\dot{\omega}}_{C_o} \left(\frac{p}{p_o}\right)^{\alpha}$, where $\bar{\dot{\omega}}_{C_o}$ is the tabulated source term computed at p_o.

The scaling exponent α was estimated from an analysis of the pressure dependance of $\bar{\dot{\omega}}_C$ computed from a set of flamelet solutions. For hydrogen chemistry, it was found that $\alpha \approx 2$, which is explained by the predominance of two-body reactions in the oxidation of hydrogen.

The chemistry model is based on an improved version of the GRI-Mech v3.0 mechanism and consists of 9 species and 28 reactions. Details on its implementation are reported in Terrapon *et al.* (2009).

4. OH LIF model

A simplified two-level model is used to simulate the OH LIF signal from RANS and LES calculations.The model is introduced to approximately account for temperature, composition, and collisional quenching effects on OH LIF. These factors limit the interpretation of the signal, especially in the context of a direct comparison with numerical simulations. With this approach, a more consistent comparison of measured and simulated quantities can be attempted.

4.1. *Two-level model*

Laser-induced fluorescence is comprised of two stages: absorption of radiation to an upper quantum state, followed by relaxation back to the ground state (Eckbreth 1996). The two-level LIF model (e.g., Eckbreth 1996) approximates this process and is constructed to approximately describe the excitation/collection scheme used in the experiment.

Taking a rovibronic transition to occur between quantum states 1 and 2, the LIF signal S_f in the linear, quenching-dominated limit (neglecting predissociation, photoionization, and line-shape effects) is $S_f \sim \chi_{OH} f_{B,1} B_{12} \frac{A_{21}}{Q_{21}} I_\nu$. In this expression χ_{OH} is the OH mole fraction; B_{12} and A_{21} are the absorption and spontaneous emission coefficients for the selected rovibronic transition; $Q_{21} = \sum_i \chi_i \hat{\sigma}_i \langle v_i \rangle$ is the total collisional quenching rate between all collisional partners of mole fraction χ_i ($\hat{\sigma}_i$ is the collisional cross-section, $\langle v_i \rangle$ is the mean relative speed); I_ν is the incident laser irradiance; and $f_{B,1}$ is the Boltzmann population fraction of the lower quantum state. For reacting flows, the pool of collisional partners changes locally based on the progress of reaction, i.e., Q_{21} locally depends on the local instantaneous chemical composition. It is therefore derived from the solution of the combustion model. Note that S_f depends linearly on the OH mole fraction but it also depends on local temperature and composition through $f_{B,1}$ and Q_{21}, which might render the interpretation of S_f as a tracer of χ_{OH} ambiguous.

5. Results

5.1. *Flow structure as visualized by the experiment*

The global structure of the flow and burning regions are found to depend on the momentum flux ratio J. Details on how these features change with J can be found in Gamba *et al.* (2011). Here, only the case of $J = 5.0$ will be discussed.

The typical shock and jet structure observed in transverse jets in supersonic crossflow is shown in Figure 3, where a time-averaged (20 μs exposure) Schlieren image of the transverse jet at $J = 5.0$ is shown (in all figures, the crossflow is from left to right). Some of the more important shock structures that were schematically shown in Figure 1 can be recognized, such as: (i) the bow shock curving around the jet, (ii) the separation oblique shock, (iii) the deformed barrel shock that terminates in the Mach disk, (iv) the re-compression shock on the lee-side of the transverse jet, and (v) the outline of the shear layer of the jet. Note also that the incoming boundary layer is rendered by the imaging technique as the thin bright layer which, at the position of the separation shock, appears to fold up as it undergoes separation.

The 3D bow shock has a strong impact on the flow and flame structure (Gamba *et al.* 2011). The bow shock inevitably interacts with the incoming boundary layer which, in response, separates, especially in laminar boundary layers (Dowdy & Newton 1963; Rogers 1971*a*,*b*). As a result, a thin recirculation region forms in front of the jet which sustains a separation shock (see Figure 3). The strength and size of these flow features are related to the level of blockage and to the strength of the induced bow shock, which are related to J. Downstream of the injection port the outline of the wake of the jet is visible and it is not affected by significant shocks. In fact, the pressure distribution in the wake quickly recovers to the undisturbed value (Everett *et al.* 1998; Gruber & Goss 1999).

Figure 4 shows a time-integrated (200 μs) OH^* chemiluminescence image of the jet at $J = 5.0$ and shows the overall ignition and flame characteristics of the system. For $J = 5.0$, burning in the shear layer, in the wake of the jet close to the wall and upstream of the injection port near the wall, is observed. This latter feature has been associated with the reacting upstream recirculation region, which acts as a stabilization mechanism (Huber *et al.* 1979). Independently of the value of J, experimental observation found that most of the OH^* was detected close to the wall rather than in the shear layer.

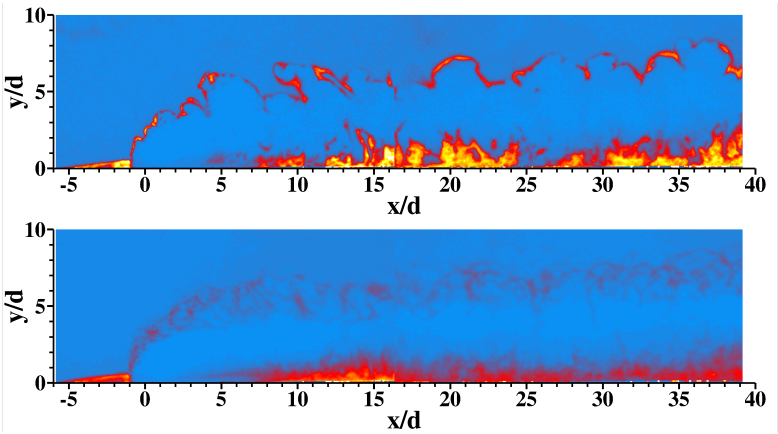

FIGURE 5. Instantaneous (top) and 11-frame average (bottom) OH PLIF image for the $J = 5.0$ case on the $x - y$ symmetry plane.

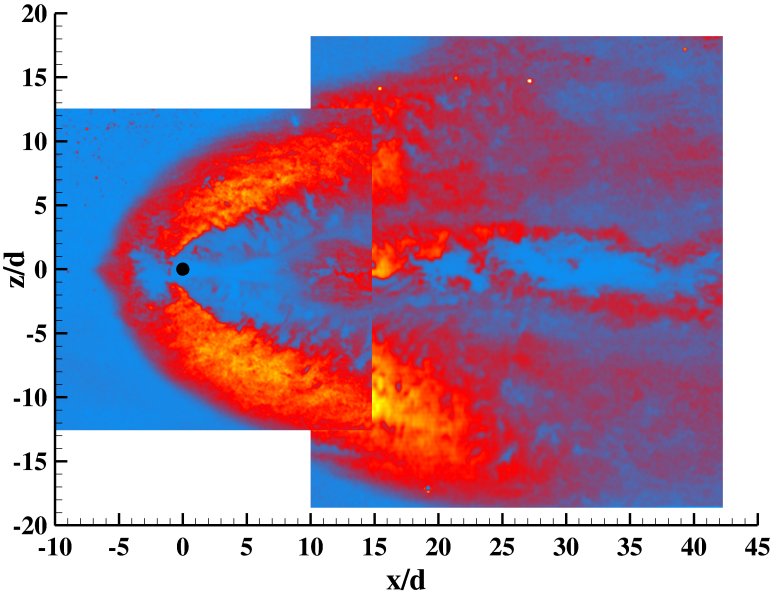

FIGURE 6. Instantaneous OH PLIF image for the $J = 5.0$ case on a $x - z$ plan-view $0.25d$ off the flat plate.

5.2. *OH PLIF visualization of the reaction zone and burning regions*

OH PLIF imaging was carried out on several orthogonal planes to identify the instantaneous reaction zone (Gamba *et al.* 2011). However, only imaging results on the symmetry side-view plane and on a plan-view plane at $0.25d$ off the wall are considered here.

Figure 5 shows an example of the instantaneous reaction zone marked by OH PLIF for the symmetry plane of the transverse jet. An 11-frame average OH PLIF image is also shown in the figure. For this high value of J, three major flow features are observed: (i) a stable reacting recirculation region upstream of the jet, (ii) a reactive shear layer on the windward side of the transverse jet, and (iii) a highly reactive boundary layer. This latter feature is clearly identified by the plan-view imaging of Figure 6 and it is found to

extend laterally for several jet diameters off the jet centerplane. Furthermore, the near-wall burning region is observed to be the dominant feature over a wide range of J values (Gamba *et al.* 2011). It seems reasonable to conclude that the intense near-wall burning observed from OH^* chemiluminescence is primarily due to the dominant OH regions near the wall shown in Figure 6. On the contrary, the combustion zones in the shear layer are localized, intermittent, thin, convoluted and with extinction-induced discontinuities. This intermittent, thin flame structure is then responsible for the weak OH^* distribution as identified above.

It is interesting to note that, although the transverse jet is immersed in a supersonic crossflow and is characterized by a jet exit Reynolds number on the order of 3.2×10^5, the instantaneous reaction zone in the shear layer of the jet is confined in thin, laminar-like, convoluted structures which resemble the structure of low-speed nonpremixed flames. This gives some support to a description of the combustion process using a flamelet-based approximation as in the FPV combustion model of Terrapon *et al.* (2009). On the other hand, regions near the wall (Figure 6) are characterized by broad and diffuse OH regions that enfold the base of the jet and their morphology depends on J. In these regions, the traditional form of the flamelet approximation might not be the most accurate combustion model, and further work is required to assess it.

5.3. *LES and RANS predictions*

After describing the structure of the burning regions as observed in the experiments, we will now consider LES and RANS predictions of this configuration (Saghafian *et al.* 2011). In this section, the results of the RANS simulation with a laminar incoming boundary layer is considered first; the turbulent boundary layer case is considered in the next section. For consistency with the experiment, the results (T and χ_i) of the computations were converted to an equivalent simulated OH LIF signal.

Figure 5.3 shows the instantaneous distribution of OH mole fraction from the LES computation (top) compared to the simulated OH LIF (bottom). Both quantities reveal the same morphological structure of the reacting jet, and there are only minor differences in the relative distribution of the OH mole fraction values and simulated OH LIF signal. In particular, some of the variation that exists in OH mole fraction going from the near-field to the far-field (in the shear layer but also in the wake near the wall) is attenuated. Overall, however, the OH PLIF is able to reproduce the main characteristics of the OH layers and the relative distribution across the measurement plane.

The results of Figure 5.3 show that many features observed in the experiments (Figure 5) are captured by the LES computation. In particular, the long, reacting recirculation region standing in front of the jet is predicted, along with the structure of the wind-ward side of the shear layer. However, the LES solution indicates intense OH LIF regions just downstream of the injector near the wall that are not observed in the experiment. This discrepancy could result from temperature and pressure effects that are currently not accounted for in the combustion model. In fact, the lee-side region of the jet experiences lower temperatures and pressures as the (cold) fuel jet exits the injector and undergoes further expansion.

The mole fraction distribution of OH on the symmetry plane as computed by the RANS model is shown in Figure 8, and it has been converted to simulated OH LIF signal in Figure 9. As it was observed for the LES simulation, OH mole fraction and simulated OH LIF signal indicate, for the most part, the same structures. Simulation shows higher OH mole fraction in the near-wall wake than in the shear layer. This difference is then attenuated once the OH mole fraction has been converted to simulated OH LIF signal.

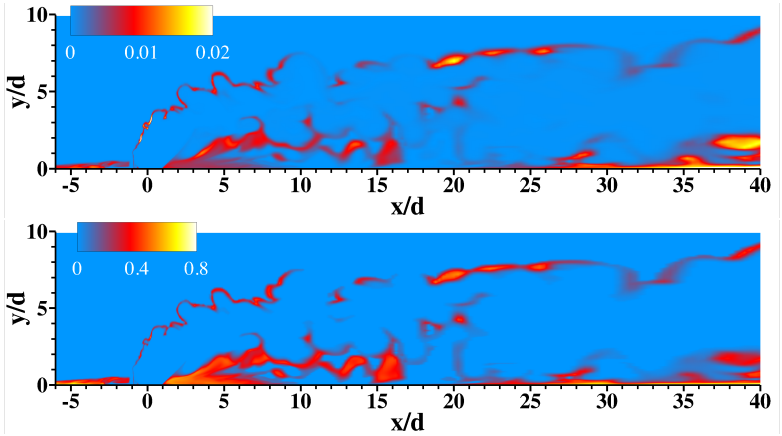

FIGURE 7. LES simulation of the $J = 5.0$ jet: instantaneous OH mole fraction (top) compared to simulated OH LIF (bottom) on the symmetry plane.

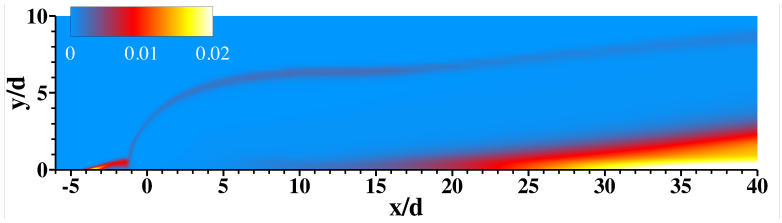

FIGURE 8. RANS simulation of the $J = 5.0$ jet: OH mole fraction on the symmetry plane.

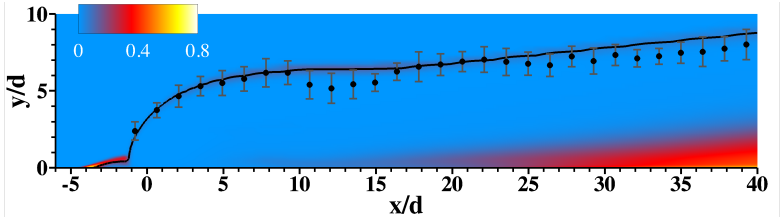

FIGURE 9. RANS simulated OH LIF with stoichiometric contour (solid line) and average location of the OH layers extracted from measurements (symbols).

Compared to experiments and LES prediction, the results of Figure 9 show that a few morphological differences exist. First, the reacting recirculation region upstream of the jet is shorter and less full than what was observed above. Furthermore, when compared to the experiment in Figure 5, the shear layer thickness is less pronounced. The latter discrepancy is a result of the RANS model being incapable of capturing the intermittency and complexity of the shear layer. Nevertheless, the RANS model well captures the overall penetration of the transverse jet. This was assessed in Figure 9 by comparing the stoichiometric contour (shown as the solid line and which compares well with the location of local maximum OH mole fraction) with the average location of the OH layers (shown as symbols) extracted from the OH PLIF imaging experiments. The RANS model reproduces with reasonable accuracy the penetration and deflection trajectory of the mean location of the reaction zone in the near field and well approximates it further downstream into the wake of the jet.

The structure of the reacting zones near the wall predicted by LES and RANS approaches will now be investigated. Figure 10 shows the instantaneous structure of the OH zones on the $0.25d$ plan-view plane as visualized in the experiment (top half) and predicted by the LES simulation (bottom half). The LES captures well the upstream extent of the recirculation region and also the overall structure of the broad OH zones. The lateral extent, however, is over-predicted. The curved, solid line in Figure 10 (on the left side of the domain) outlines the foot of the bow shock, which is defined as the points on the imaging plane extracted from the simulation at which pressure is 10% above the freestream value. Comparison of the shock foot location with the upstream envelope of the OH layers supports the idea introduced previously that the near-wall OH structure might be driven by the fluid dynamic interaction of the bow shock with the jet and the incoming boundary layer. The processes resulting from the interaction would then sustain and enhance entrainment and mixing, and would allow for longer flow residence times.

The RANS prediction of the near-wall burning regions is shown in Figure 11. Contrary to the LES model, the RANS simulation tends to under-predict the size of the upstream recirculation region and the lateral spreading of the OH zones near the wall. Furthermore, the bow shock foot predicted by RANS indicates a bow shock somewhat narrower than the LES prediction and which does not envelope the OH distribution predicted by the RANS simulation. The RANS predicted location of the shock foot, however, agrees well with the location of the diffuse OH zone observed in the experiments. Note that in the experiment the location of the shock foot is not known. However, the favorable agreement of the side-view location of the bow shock (i.e., Figure 3) predicted by RANS and observed in the experiment (not shown) supports the assumption that RANS might be able to capture the overall 3D structure of the bow shock and of the flow around the jet. Therefore, the shock foot location predicted by RANS might be used as an approximate marker of the location of the shock foot in the experiment. These results provide reason to assume that the lateral extent of the near-wall burning region is driven by the bow shock/boundary layer interaction around the jet. The following section further investigates how this feature is influenced by the characteristics of the incoming boundary layer and bow shock.

5.4. *Effect of boundary layer on near-wall burning regions*

Comparison of the characteristics of the OH regions predicted by LES and RANS with experimental observation has identified key differences in the near-wall region. In this region, both experiments and LES indicate lateral OH zones bounded upstream by the bow shock. On the contrary, the RANS prediction shows a more narrow OH distribution near the wall which does not follow the location of the bow shock. However, the RANS calculation was performed with a rather crude approximation of the more complex laminar/turbulent transition that might occur at the bow shock foot in the experiment (recall that the transition point in RANS was imposed at the location of the recirculation bubble). If the near-wall OH region results from the bow shock/boundary layer interaction, it seems plausible that the outcome is sensitive to details of the incoming boundary layer and its modeling. This could explain the large difference observed in the RANS results. Although it is not clear at this stage whether these near-wall burning regions are dynamically important in a global sense (for example, they might have a limited contribution to the energy deposition into the flowfield), it is important to understand the link between their characteristics and the characteristics of the boundary layer. Because the RANS results are inconclusive, it is also important to understand the ability (or limitations) of

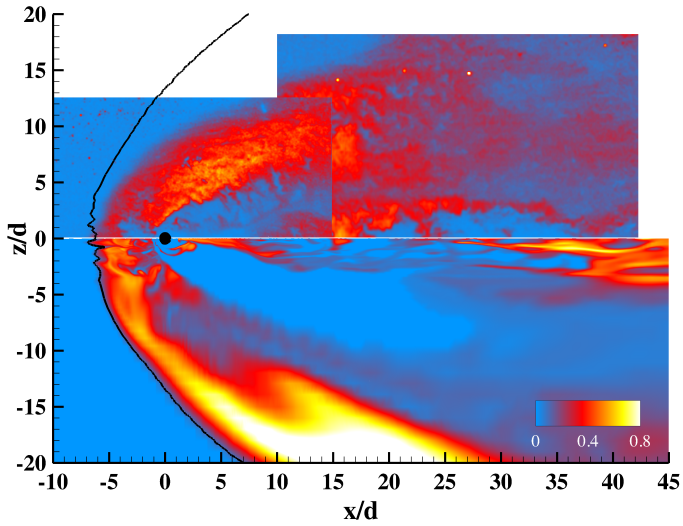

FIGURE 10. LES of the $J = 5.0$ jet: instantaneous simulated OH LIF (bottom half) on the $0.25d$ plan-view plane compared to experiment (top half). Solid line indicates shock foot location in the LES simulation.

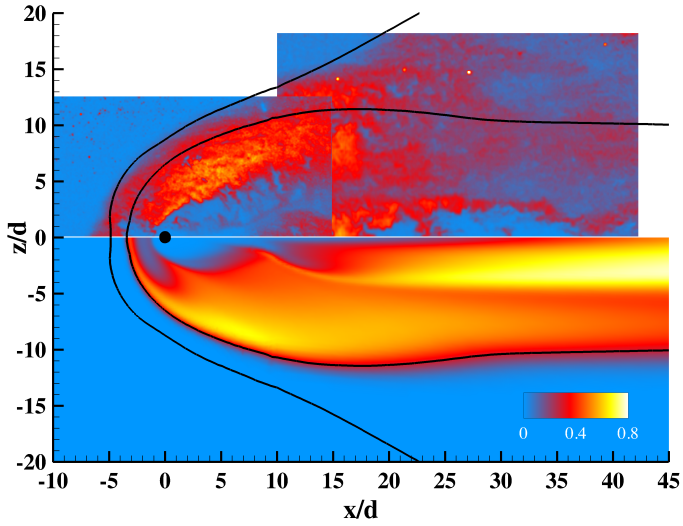

FIGURE 11. RANS of the $J = 5.0$ jet: simulated OH LIF (bottom half) on the $0.25d$ plan-view plane compared to instantaneous experiment (top half). Outer solid line: shock foot location from RANS; inner solid line: $Z = 0.005$ iso-contour line.

RANS to capture these processes that might be critical in other regions, under different conditions, or in cases where shock/flow interaction dominates the flowfield and the combustion process. In order to assess these aspects further, additional imaging experiments were carried out with a turbulent boundary layer generated by tripping the flow near the leading edge of the flat plate. Additional RANS calculations assuming a fully turbulent boundary layer from the leading edge were also performed for comparison.

Figure 12 shows the instantaneous OH distribution near the wall ($0.25d$) visualized

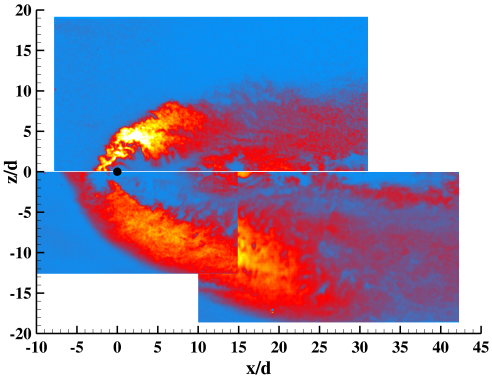

FIGURE 12. Effect of laminar (bottom half) and turbulent (top half) boundary layer on near-wall ($0.25d$) OH distribution as visualized by OH PLIF in the experiment.

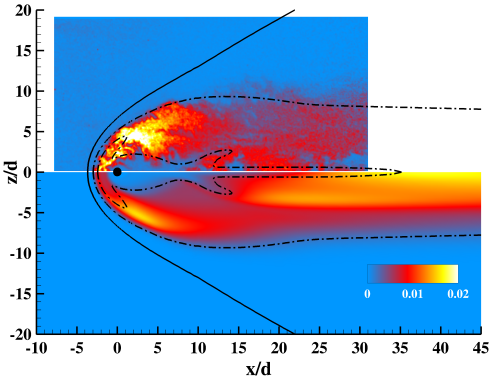

FIGURE 13. Effect of turbulent boundary layer on near-wall ($0.25d$) OH distribution of $J = 5.0$ jet. RANS simulation (bottom half) and OH PLIF (top half). Solid line: bow shock foot; dash lines stoichiometric and $Z = 0.005$ contours.

by OH PLIF for the case of a turbulent (top half) and laminar (bottom half) incoming boundary layer, respectively. As demonstrated by these results, the incoming boundary layer has a strong impact on the near-wall burning regions. For example, the near-wall OH zone for a turbulent boundary layer is more confined around the injector than for a laminar boundary layer. The length of the upstream recirculation region (a characteristic size of this feature) is found to be about three times smaller for the turbulent case than for the laminar one.

Figure 13 shows a comparison of the instantaneous OH zones near the wall at $0.25d$ with a turbulent boundary layer observed in the experiment (top half) with RANS prediction (bottom half). The shock foot (solid line) and two iso-contour (dash) lines of the mixture fraction are also shown. In this case, RANS well replicates the size and location of the OH zones seen in the experiment. The outer dash line defining the $Z = 0.005$ iso-contour line well bounds the OH zones in both the RANS calculations and experiment. Furthermore, many other details of the OH distribution are well predicted. For example, both the RANS calculation and the experiment found a high OH mole fraction (OH LIF signal) in the upstream portion of the reacting horse-shoe region around the injector which then decreases downstream. In both cases there is a low OH mole fraction region just downstream of the injector which ends at the lee-ward side reattachment point. The main difference is in the regions downstream of the reattachment point where the high OH mole fraction region predicted by RANS near the centerline is not observed in the experiment. In general, it seems that RANS could be a viable approach to predict even these complex regions.

6. Conclusions

This work investigates the structure of the reaction zones of hydrogen transverse jets in supersonic crossflow. The final objective is to provide an assessment of the supersonic combustion model of Terrapon *et al.* (2009) and Saghafian *et al.* (2011) implemented in LES and RANS solvers by simulating the experiment of Gamba *et al.* (2011).

In the experiments, the flame structure was visualized by OH PLIF on the symmetry

side-view plane and on a plan-view plane $0.25d$ off the wall. The experimental work identified thin, convoluted, laminar-like OH layers in the shear layer of the jet and broad OH regions near the wall within the boundary layer. These latter regions are believed to result from the upstream separation region and horse-shoe vortex system developing around the base of the jet in combination with the interaction of the bow shock with the incoming laminar boundary layer. The structure of the near-wall burning region was also found to depend strongly on the incoming boundary layer (laminar or turbulent).

The LES simulation well captures the spatial distribution, structure and intermittency of the reacting layers found in the experiments. However, the LES computation showed an overestimation of the OH zone structure at the wall, which might be due to compressibility effects not fully accounted for in the combustion model. On the other hand, the RANS simulation well predicts the flame penetration into the crossflow, and the lateral extent of the OH region close to the wall for turbulent incoming boundary layers, but under-predicts the broadening of the shear layer induced by the large-scale intermittency.

In the laminar boundary layer case, the RANS approach was not able to predict the correct dynamics of the interaction between the bow shock and the incoming boundary layer, resulting in a large under-prediction of the lateral extent of the near-wall burning region in this case. This was shown to be directly related to the ad-hoc treatment of transition, where the turbulence model was simply turned on at a fixed location upstream of the injection. It might be conjectured that a more adequate model of the transition process could improve those results. Although it is not clear whether the observed near-wall burning regions are important to the overall energy deposition budget (other than possibly being an important flame stabilization and flame-holding mechanism), these results highlight the sensitivity on the incoming boundary layer of the processes that might be most important to mixing, entrainment and flame stability near walls and under conditions when shock/flow interaction is important. Because under realistic conditions of a supersonic combustor turbulent flow is more likely, the shortcomings of the RANS model and sensitivity to the details of laminar flow conditions might not play a significant role.

In light of these results, we can conclude that the proposed combustion model shows promise for both RANS and LES, and is able to capture the key features observed in the experiment. Future work will focus on further improvements of the model to account for compressibility effects.

Acknowledgments

This material is based upon work supported by the Department of Energy under the Predictive Science Academic Alliance Program (PSAAP) at Stanford University, Award Number(s) DE-FC52-08NA28614. The authors would like to thank Catherine Gorle for useful discussion during drafting of this manuscript.

REFERENCES

Barth, T. J. & Jespersen, D. 2011 The design and application of upwind schemes on unstructured meshes. In *Paper No. AIAA-1989-0366*.

Batten, P., Leschziner, M. A. & Goldberg, U. C. 1997 Average-state Jacobians and implicit methods for compressible viscous and turbulent flows. *J. Comput. Phys.* **137** (1), 38–78.

Dowdy, M. W. & Newton, J. F. 1963 Investigation of liquid and gaseous secondary injection phenomena on a flat plate with M=2.01 to M=4.54. *Tech. Rep.*. JPL Technical Report No. 32-542.

Eckbreth, A. C. 1996 *Laser Diagnostics for Combustion Temperature and Species*, 2nd edn. Gordon and Breach Publishers.

Everett, D. E., Woodmansee, M. A., Dutton, J. C. & Morris, M. J. 1998 Wall pressure measurements for a sonic jet injected transversely into a supersonic crossflow. *J. Propul. Power* **14** (6), 861–868.

Gamba, M., Mungal, M. G. & Hanson, R. K. 2011 Ignition and near-wall burning in transverse hydrogen jets in supersonic crossflow. In *49th AIAA Aerospace Sciences Meeting and Aerospace Exposition, Jan. 4-7, Orlando, Florida, AIAA Paper No. AIAA-2011-0319*.

Gruber, M. R. & Goss, L. P. 1999 Surface pressure measurements in supersonic transverse injection flowfields. *J. Propul. Power* **15** (5), 633–641.

Ham, F. & Iaccarino, G. 2004 Energy conservation in collocated discretization schemes on unstructured meshes. In *Center for Turbulence Research, Annual Research Briefs*, pp. 3–14.

Heltsley, W. N. 2011 Structure and stability of reacting jets in supersonic crossflows. PhD thesis, Department of Mechanical Engineering, Stanford University.

Heltsley, W. N., Snyder, J. A., Houle, A. J., Davidson, D., Mungal, M. G. & Hanson, R. K. 2006 Design and characterization of the Stanford 6 inch Expansion Tube. In *42nd AIAA/ASME/SAE/ASEE Joint Propulsion Conference & Exhibit, 9 - 12 July, AIAA Paper No. AIAA-2006-4443*.

Huber, P. W., Schexnayder, C. J. & McClinton, C. R. 1979 Criteria for self-ignition of supersonic hydrogen-air mixtures. *Tech. Rep.*. NASA TP-1457.

Mahesh, K., Constantinescu, G. & Moin, P. 2004 A numerical method for Large-Eddy Simulation in complex geometries. *J. Comput. Phys.* **197**, 215–240.

Menter, F. R. 1994 Two-equation eddy-viscosity turbulence models for engineering applications. *AIAA J.* **32** (8), 1598–1605.

Moin, P., Squires, K., Cabot, W. & Lee, S. 1991 A dynamic subgrid scale model for compressible turbulence and scalar transport. *Physics of Fluids A* **3**, 2746–2757.

Moureau, V., Bérat, C. & Pitsch, H. 2007 An efficient semi-implicit compressible solver for large-eddy simulations. *J. Comput. Phys.* **226**, 1256–1270.

Pecnik, R., Terrapon, V. E., Ham, F. & Iaccarino, G. 2009 Full system scramjet simulation. In *Center for Turbulence Research, Annual Research Briefs*, pp. 33–45.

Peters, N. 1984 Laminar diffusion flamelet models in non-premixed turbulent combustion. *Prog. Energy Combust. Sci.* **10**, 319–339.

Pierce, C. D. & Moin, P. 2004 Progress-variable approach for Large-Eddy Simulation of non-premixed turbulent combustion. *J. Fluid Mech.* **504**, 73–97.

Pitsch, H. 2006 Large-eddy simulation of turbulent combustion. *Annu. Rev. of Fluid Mech.* **38**, 453–482.

Rogers, R. C. 1971*a* Mixing of hydrogen injected from multiple injectors normal to a supersonic airstream. *NASA TN D-6476* .

Rogers, R. C. 1971*b* A study of the mixing of hydrogen injected normal to a supersonic airstream. *NASA TN D-6114* .

Saghafian, A., Terrapon, V. E., Ham, F. & Pitsch, H. 2011 An efficient flamelet-based combustion model for supersonic flows. In *Paper No. AIAA-2011-2267, 17th*

AIAA International Space Planes and Hypersonic Systems and Technologies Conference, April 11-14, San Francisco.

Satish, B., Buschelman, K., Eijkhout, V., Gropp, W. D., Kaushik, D., Knepley, M. G., McInnes, L. C., Smith, B. F. & Zhang, H. 2009 Petsc. In *Web page, http://www.mcs.anl.gov/petsc*.

Shoeybi, M., Svard, M., Ham, F. & Moin, P. 2010 An adaptive implicit-explicit scheme for the DNS and LES of compressible flows on unstructured grids. *J. Comput. Phys.* **229**, 5944–5965.

Terrapon, V. E., Ham, F., Pecnik, R. & Pitsch, H. 2009 A flamelet-based model for supersonic combustion. In *Center for Turbulence Research, Annual Research Briefs*, pp. 47–58.

Terrapon, V. E., Pecnik, R., Ham, F. & Pitsch, H. 2010 Full-system rans of the hyshot ii scramjet, part 2: Reactive cases. In *Center for Turbulence Research, Annual Research Briefs*, pp. 69–80.

Toro, E. F., Spruce, M. & Spears, W. 1994 Restoration of the contact surface in the HLL-Riemann solver. *Shock Waves* **4**, 25–34.

Trimpi, R. L. 1962 A preliminary theoretical study of the expansion tube, a new device for producing high-enthalpy short-duration hypersonic gas flows. *Tech. Rep.*. NASA TR R-133.

Venkatakrishnan, V. 1995 Convergence to steady state solutions of the euler equations on structured grids with limiters. *J. Comput. Phys.* **118**, 120–130.

White, F. M. 1991 *Viscous Fluid Flow*. McGraw Hill.